Quantitative Chemical Imaging of the Intracellular Spatial Distribution of Fundamental Elements and Light Metals in Single Cells

Emil Malucelli,[†] Stefano Iotti,*[,†,◆] Alessandra Gianoncelli,[§] Michela Fratini,[‖] Lucia Merolle,[†] Andrea Notargiacomo,[⊥] Chiara Marraccini,[#] Azzurra Sargenti,[†] Concettina Cappadone,[†] Giovanna Farruggia,[†,◆] Inna Bukreeva,[⊥] Marco Lombardo,[‡] Claudio Trombini,[‡] Jeanette A. Maier,[∇] and Stefano Lagomarsino[○,◆]

[†]Department of Pharmacy and Biotechnology, University of Bologna, Bologna 40127, Italy

[‡]Department of Chemistry "G. Ciamician", University of Bologna, Bologna 40126, Italy

[§]Elettra - Sincrotrone Trieste, 34149 Basovizza, Trieste, Italy

[‖]"Enrico Fermi" Centre MARBILab , c/o Fondazione Santa Lucia, Via Ardeatina, 306, 00179 , Roma, Italy

[⊥]Institute for Photonics and Nanotechnology, Consiglio Nazionale delle Richerche, 00156 Rome, Italy

[#]Department of Life Sciences, University of Modena e Reggio Emilia, 41125 Modena, Italy

[∇]Department of Biomedical and Clinical Sciences "L. Sacco", University of Milan, 20157 Milan, Italy

[○]Institute of Chemical-Physical Processes, Sapienza University of Rome, 00185 Rome, Italy

[◆]National Institute of Biostructures and Biosystems, 00136 Rome, Italy

S *Supporting Information*

ABSTRACT: We report a method that allows a complete quantitative characterization of whole single cells, assessing the total amount of carbon, nitrogen, oxygen, sodium, and magnesium and providing submicrometer maps of element molar concentration, cell density, mass, and volume. This approach allows quantifying elements down to 10^6 atoms/μm^3. This result was obtained by applying a multimodal fusion approach that combines synchrotron radiation microscopy techniques with off-line atomic force microscopy. The method proposed permits us to find the element concentration in addition to the mass fraction and provides a deeper and more complete knowledge of cell composition. We performed measurements on LoVo human colon cancer cells sensitive (LoVo-S) and resistant (LoVo-R) to doxorubicin. The comparison of LoVo-S and LoVo-R revealed different patterns in the maps of Mg concentration with higher values within the nucleus in LoVo-R and in the perinuclear region in LoVo-S cells. This feature was not so evident for the other elements, suggesting that Mg compartmentalization could be a significant trait of the drug-resistant cells.
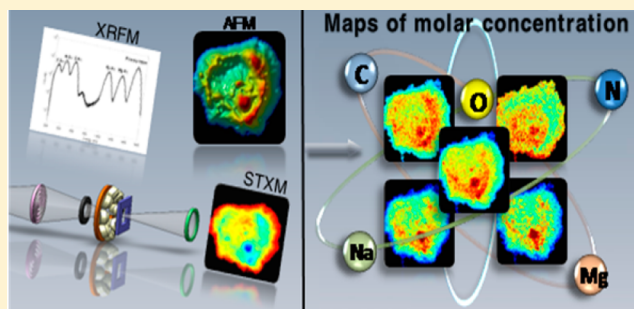
Knowledge of the spatial distribution and concentration of elements in cells is a challenging issue to reach. A detailed picture of the intracellular distribution of the fundamental life elements (FLE) constituting the molecules of living systems—carbon (C), nitrogen (N), and oxygen (O)—is still lacking. Moreover, other elements, such as light metals, play a fundamental role. Indeed, many basic aspects and regulatory mechanisms of cell functions are related to the intracellular compartmentalization of ions, whose different concentration gradients generate the electrical potentials that are the driving forces of many cellular processes. "How much? and where is it?" represents one of the archetypal questions essential in science.

To answer the first question, a proper way must be chosen to express and measure the amounts of a given element: this issue is not trivial. We emphasize the importance of mapping the elemental distribution in molar concentration, which necessarily requires to measure both mass and volume. The concentration expressed in molarity refers to the concept of mole used in chemistry instead of units of mass. Indeed, knowledge of the mass of each of the components in a chemical system is not sufficient to define the system. It is part of the history of science that the introduction of the concept of mole

was paradigmatic, giving a substantial contribution to translate chemistry from alchemy to science.

The spatial identification and characterization of the chemical composition level in a whole cell (chemical imaging) is a demanding task because it requires analytical methods with high elemental sensitivity, specificity and high spatial resolution. Today there are several electron, proton, and synchrotron X-ray[1] and ion (nano secondary ion mass spectroscopy)[2] microprobe techniques for elemental imaging, speciation, and quantification in single cells. All these standardless quantification techniques, capable of measuring both the amount of elements and the local mass of the sample, give the opportunity to obtain a chemical imaging of cells. Nevertheless, they measure the amounts of the element in mass fraction and not in molar concentration, being unable to determine the volume of the sample unless the density is known and uniform, which is obviously not the case in cells.

In principle, X-ray fluorescence tomography is certainly a very elegant way to solve the problem, but the very high radiation exposure implicit in this technique makes it difficult to apply to cells, like mammalian ones, not provided with external shield as diatoms.[3] Moreover, quantitative compositional information can be obtained by X-ray fluorescence microscopy (XRFM) alone but only in the case of uniform thickness, as in sections,[4] but not in the whole cell.

Recently, we provided a proof of the feasibility of combining XRFM and atomic force microscopy (AFM) to merge local elemental composition and morphological information (volume) providing a Mg distribution map.[5] However, in this previous work we used, as "external standard", the intracellular average content of Mg assessed by a fluorescent chemosensor in a population of similar cells.[6] Therefore, mapping at submicrometer level the absolute molar concentration of FLE and light metals in whole cells is a goal that still remains to be reached.

The aim of this paper is to present a comprehensive method that provides directly the elemental molar concentration, implementing a modified equation of the fundamental parameter[7] approach to the aforementioned method,[5] and extending the analysis to FLE in addition to light metals such as magnesium (Mg) and sodium (Na). Quantification of the light elements at high spatial resolution is a particularly challenging issue, since their low atomic number entails two major inconveniences: low X-ray fluorescence yield and strong absorption of fluorescence radiation by the cell itself (self-absorption).[7] Probably for these reasons, FLE and light metals have neither been mapped nor quantified in cells by XRFM, despite their importance in fundamental biological processes.

To overcome these difficulties we combined XRFM, AFM, and scanning transmission X-ray microscopy (STXM), providing the first molar concentration map of FLE and the light metals Na and Mg in whole dehydrated cells ("how much") and also obtaining submicrometer spatial distribution of the cell mass, density, and volume ("where is it"). Then the quantification of the total mass, density, and volume of single cells together with the total molar concentration of each element is given.

■ EXPERIMENTAL SECTION

Cell Preparation. In this work we studied two different cell lines: osteoblast U2OS cells and two strains of human colon carcinoma cells LoVo, sensitive (LoVo-S) and resistant (LoVo-R) to doxorubicin (donated by Dr. P. Perego, Istituto Nazionale Tumori, Milano). Cell lines were cultured in Roswell Park Memorial Institute (RPMI) medium and Dulbecco's modified Eagle's medium (DMEM) medium (Sigma), respectively, supplemented with 10% fetal bovine serum (FBS), 2 mM glutamine, 100 units/mL penicillin, and 100 μg/mL streptomycin sulfate. LoVo doxorubicin-resistant cells (LoVo-R) were cultured under the same conditions and fed once every 2 weeks with 1 μg/mL doxorubicin. Doxorubicin (Sigma) was prepared fresh in sterile ultrapure water at desired concentration. For atomic force microscopy and X-ray measurements, cells were plated at a concentration of 1 × 10⁴ cell/cm² on 1 × 1 mm², 200-nm-thick silicon nitride (Si_3N_4) membrane windows, mounted on a 5 × 5 mm² Si frame (Silson) previously sterilized in ethanol. Cells were incubated at 37 °C in 5% CO_2 for at least 24 h. Two dehydration methods were then followed. In the first case, at 50−80% confluency, cells were briefly rinsed in 150 mM KCl and then fixed in ice-cold methanol/acetone 1:1 and air-dried. In the second case, after being rinsing with 100 mM ammonium acetate, cells were cryofixed by plunge freezing in liquid ethane[8] and then dehydrated in vacuum at low temperature overnight.

Atomic Force Microscopy Measurements. Cell thickness maps were collected on a Digital Instruments D3100 AFM equipped with a Nanoscope IIIa controller. Measurements were carried out in air in Tapping Mode at a resonance frequency of about 260 kHz by use of monolithic silicon tips with an apex curvature radius in the 5−10 nm range and a typical force constant of ∼40 N·m⁻¹. The typical square scan size used was on the order of 50 μm × 50 μm, and the matrix resolution in pixels was 512 × 512. A careful choice of scanning parameters (including scan size and angle, tip speed, feedback setpoint, and gains) was made in order to prevent artifacts and/or cell damage; images were collected without filtering or flattening and were completely postprocessed.[5] In order to obtain quantitative thickness maps, AFM height data were corrected for the substrate level offset and tilt: this required that we set the scan size much larger than the cell dimension, that is, to have at least a 10-μm-wide substrate surface surrounding the cell in the image. The cell thickness at each pixel was then estimated as the height measured with respect to the substrate level. The uncertainty associated with AFM measurements of cell thickness was estimated in about 30 nm, although this value may be overestimated, in particular when the measured thickness is small.[9]

X-ray Fluorescence Microscopy and Scanning Transmission X-ray Microscopy Setup. The XRFM and STXM measurements were carried out at the beamline Twinmic[10] at Elettra Synchrotron (Trieste, Italy). Figure S1 in Supporting Information shows schematically the Twinmic setup. A Fresnel zone plate focused the incoming beam (1475 eV), monochromatized by a plane grating monochromator, to a circular spot of about 600 nm in diameter. The sample was transversally scanned in the zone plate focus, in steps of 500 nm. At each step the fluorescence radiation intensity was measured by eight Si-drift detectors (active area 30 mm²)[11] concentrically mounted at a 20° grazing angle with respect to the specimen plane, at a detector-to-specimen distance of 28 mm. Simultaneously, the transmitted intensity T was measured by a fast-readout electron-multiplying low-noise charge-coupled device (CCD) detector through an X-ray−visible light converting system.[12] Zone plate, sample, and detectors were in vacuum, thus avoiding any absorption and scattering by air.

Acquisition Protocol. Dehydrated cells mounted on the Si_3N_4 membrane windows were carefully examined with optical microscope and selected following these criteria: integrity, dimensions (large cells require longer acquisition time), and distance from other cells (clustered cells have been avoided because AFM measurements require some free space around the cells). AFM measurements were performed on selected cells before and after XRFM and STXM measurements. Five STXM images were acquired on whole cells with 25 ms dwell time per step, with a step size of 500 nm. In sequence XRFM, and simultaneously also STXM, were carried out with a range of 6−8 s dwell time per pixel depending on the cell size. The total acquisition time was in the range of 5−8 h (field of view of at least 20 × 20 μm; spatial resolution 500 nm). The measurement of I_0 is made on a part of the substrate free from cells, acquiring 25 points and repeating the measure five times. Therefore the statistical error of I_0 is much lower than the statistical error of I.

STXM Analysis. The transmission $T(t)$ as function of the thickness t is given by the Beer−Lambert law:

$$T(t) = I(t)/I_0 = \exp[-\mu(E_0)t] = \exp[-\mu_m(E_0)\rho t] \quad (1)$$

where I_0 is the initial beam intensity (expressed in photons per second per square micrometer), $I(t)$ is the intensity at a depth t into the sample, $\mu(E_0)$ is the X-ray linear absorption coefficient at incident energy E_0, $\mu_m(E_0) = \mu(E_0)/\rho$ is the mass absorption coefficient at the same energy, and ρ is the matrix density. It is often more convenient to use μ_m instead of μ, because μ_m does not depend on the aggregation state of the elements, and universal tables are available for μ_m. In the case of multielement material, the total mass absorption coefficient $(\mu_m)_{tot}$ is given by the weighted sum of the individual $(\mu_m)_i$:

$$(\mu_m)_{tot}(E_0) = \sum_i w_i(\mu_m)_i(E_0) \quad (2)$$

where w_i is the mass fraction of element i. From the measurements of transmission by use of eq 1, the ρ map (named density maps in the main text and figures) can be calculated by deriving t from the AFM measurements, and considering a given cell composition taken from literature.[13] The typical elemental cell composition values reported in literature are referred to the empirical composition on a per carbon basis for the dry weight of *Escherichia coli* which is $C:H_{1.77}:O_{0.49}:N_{0.24}$ (BioNumbers database ID BNID 101800). The mass fractions of carbon (w_C), nitrogen (w_N), and oxygen (w_O) in dehydrated cells were calculated from the above stoichiometric relationship, resulting in the values $w_C = 48\%$, $w_N = 14\%$, and $w_O = 31\%$.

The mass distribution is obtained by the simple relationship $m = \rho St$, where S is the area of a single pixel and t is the thickness obtained by AFM. This procedure requires, however, very careful registration of the thickness map recorded with AFM onto the transmission map recorded by STXM. The registration procedure is illustrated below.

XRFM Analysis. The Kα X-ray fluorescence lines of C, N, O, Na, and Mg were detected with an incident energy of about 1475 eV. The X-ray fluorescence spectra were analyzed by PyMCA software,[14] which provides for each element i the total counts R_i for the fluorescence line under consideration. To obtain quantitative information from the measurement of fluorescence radiation, we used the fundamental parameter method,[5] based on the relationship:

$$dR_i = [w_i\rho Sdz_i][Y(E_{0,i})][I_0 \exp(-\chi\rho z)] \quad (3)$$

where dR_i is the contribution to the total counts for that specific fluorescence line, given by the sample mass $dm_i = w_i\rho dV$ contained in the infinitesimal volume $dV = S\,dz$ at depth z.

$$Y(E_{0,i}) = \varepsilon_i(\Omega/4\pi)\omega_i p_i \tau(E_{0,i})$$

where ε_i is the detector efficiency, Ω is the solid angle seen by the detector, ω_i is the fluorescence yield, p_i is the transition probability, and $\tau(E_{0,i})$ is the photoelectric cross section at E_0.

I_0 is the incident intensity and

$$\chi = [\mu_m(E_0) \cosec(\alpha) + \mu_m(E_i) \cosec(\beta)] \quad (4)$$

represents the total self-absorption of primary and fluorescent radiation in the sample, where E_i is the energy of the specific fluorescence radiation of element i, $\mu_m(E_0)$ is the sample mass absorption coefficient at energy E_0 of the incident beam, α is the incident angle, $\mu_m(E_i)$ is the mass absorption coefficient at energy E_i of the specific fluorescence line, and β is the exit angle of the fluorescence radiation as seen by the detector. Equations 3 and 4 are valid in the case of samples with uniform thickness, and in this case eq 3 has an analytical solution, but for nonuniform samples, as is the case for whole cells, we must know the morphology (thickness) and density distribution of the sample to correct for self-absorption. We developed an ad hoc algorithm[15] for this task, based on AFM and STXM measurements. Absorption of the fluorescence radiation is calculated voxel by voxel, taking into account the path that the radiation has to travel inside the sample and considering the morphology measured by AFM and the local density at each point, as a result from the density map obtained by STXM. Because the detectors see the sample from eight different orientations, the calculations have been carried out independently for each detector.

In eq 3, the factor Y also contains the efficiency and the solid angle seen by the detectors. In principle they are the same for all the detectors, and therefore the corrected maps should deliver the same values, but experimentally some differences were found. To calibrate the detectors we examined two standards: one constituted by a Mg film 200 nm thick covered by 50 nm Au to protect Mg from oxidation, and the other constituted by a bare 200 nm thick Si_3N_4 window, equal to those used as substrate for our samples. The Mg Kα and N Kα lines were respectively measured in different positions of the standards and then averaged out. The thickness of the standards being uniform, the analytical solution of eq 3 can be used to compare the experimental counting rates with the expected ones. To this purpose, the incident intensity has been calibrated with a photodiode. We calculated correction factors for each detector at both the N and Mg energies, as ratios between experimental and expected rates. We used N correction factors to normalize the detector efficiency at the energies of C, N, and O in the quantitative determination of mass fraction maps of each element. The Mg correction factors were used to normalize the detector efficiency at the energies of Na and Mg.

Mass Fraction and Concentration Calculation. The mass fraction $(w_p)_i$ for each pixel p for each element i was calculated by the following expression derived from eq 3:

$$(w_p)_i = \frac{(R_p)_i}{[\rho_p V_p][Y(E_{0,i})]F_p} \quad (5)$$

where V_p is the volume of the pixel p, expressed in cubic centimeters, and F_p is the correction factor for the self-absorption of both incident beam and fluorescence radiation. Analogously, the concentration $(M_p)_i$ in the single pixel p, expressed in molarity, is derived by the following expression:

$$(M_p)_i = \frac{(m_p)_i}{A_i V_p} \times 10^3$$

$$= \frac{(w_p)_i \rho_p V_p}{A_i V_p} \times 10^3$$

$$= \frac{(R_p)_i}{[A_i V_p][Y(E_{0,i})]F_p} \times 10^3 \tag{6}$$

where m_i is the mass expressed in grams and A_i is the atomic weight of the ith element. It is evident that eq 6 is a modified version of the fundamental parameter equation (eq 5) simplified for the density ρ. As a consequence, concentrations can be directly calculated (eq 6) bypassing the calculation of mass fraction.

Images Registration. The method presented in this work is based on the multimodal fusion of heterogeneous information acquired with different techniques: synchrotron-based X-ray images (XRFM and STXM) and morphological data collected by AFM. A robust registration (alignment) procedure is necessary to deal with data collected with different imaging techniques having different spatial resolution and/or deformations. Moreover, XRFM images were affected by various degrees of deformation induced by beam instability during the long acquisition time (a few hours). An accurate registration requires us to align images with the same contrast and as much as possible with high signal-to-noise ratio. To this purpose we used as reference images the XRFM maps (Figure 2, XRFM image) of the sum of the eight detectors obtained by the program PyMCA[14] as the sum of all the channels of the XRFM spectrum acquired at each scanning step. AFM was registered onto fluorescence raw maps by use of the images registration software FLIRT (http://fsl.fmrib.ox.ac.uk/fsl/flirt/) by a 2D linear transformation with 6 degrees of freedom (1 rotation, 2 translation, 2 scale, 1 skew; i.e., oblique deformation). Registered images were then resampled by interpolating with a trilinear function. In order to improve the alignment of AFM images onto XRFM, we applied a nonlinear registration using unwarp2d program part of the Automated Registration Toolkit (ART http://www.nitrc.org/projects/art/). With the nonlinear interpolation, we decrease the misalignment due to the deformation in XRFM.

RESULTS AND DISCUSSION

In Figure 1, the flowchart of the whole analytical process from the sample preparation to the molar concentration maps is reported. A multidisciplinary approach has been adopted, with the use of complementary techniques seldom applied in combination. A well-defined procedure to obtain the elemental molar concentration maps has been elaborated, implying several stages and key steps that integrate data from different analytical techniques by the implementation of custom-made algorithms (see Experimental Section). The key steps of the procedure are (i) acquisition of fluorescence and transmission maps and of AFM topography map, (ii) alignment of the AFM map onto X-ray image space, (iii) generation of density maps, (iv) self-absorption correction, (v) generation of FLE and light
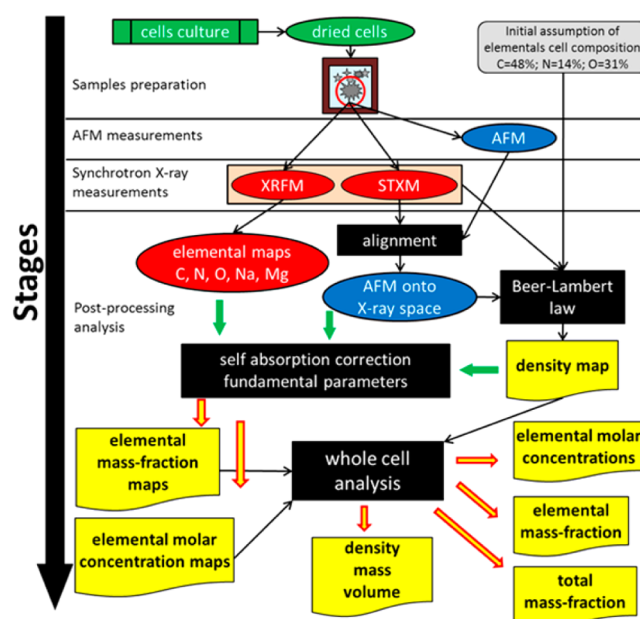

Figure 1. Flowchart in stages of the whole analytical process presented in this study. Colored boxes represent sample preparation (green), initial assumption (gray), AFM measurements and analysis (blue), X-ray measurements and analysis (red), computational steps (black), and final outputs of the analytical process (yellow).

metals molar concentration maps, and (vi) elemental quantification in whole cells (black boxes in Figure 1). The XRFM and STXM measurements were carried out at the beamline Twinmic[10] at Elettra Synchrotron (Trieste, Italy). Figure S1 in Supporting Information shows the scheme of the Twinmic setup described in the Experimental Section.

Mass, Density, Mass Fraction, and Molar Concentration Maps in Single Cells. Morphology, X-ray transmission, and raw X-ray fluorescence maps were obtained by AFM, STXM, and XRFM, respectively, in a human osteosarcoma U2OS freeze-dried cell (Figure 2, first row). A detailed map of the spatial distribution of cell density and mass was then derived by merging STXM information and cell thickness map obtained by AFM aligned onto STXM space (Figure 2, second row). Our maps are the projection in two dimensions of the 3-D real distribution. It is interesting to note the lack of a strict correspondence between the intracellular distributions of mass and density. In particular, arrows indicate the area where mass and density intracellular distributions notably differ: green arrow denotes high mass and low density area, while purple arrow indicates high mass and high density area. It is worth noting that both high mass areas correspond to cell regions of large thickness as detectable from AFM images. Moreover, the suitable combination of AFM and STXM with XRFM of each element allows us to have all the information necessary to build intracellular maps of mass fraction and molar concentration of C, N, O, Na, and Mg (Figure 2, third and fourth rows, respectively). In particular, the mass fraction and molar concentration maps were obtained by normalizing the maps of fluorescence intensity respectively with mass or volume maps (see eqs 5 and 6 in the Experimental Section). This accurate approach provides both submicrometer spatial resolution and quantification of elements down to 10^6 atoms/μm^3 (based on the minimum Mg concentration detected in a single pixel, i.e., 1 mM)
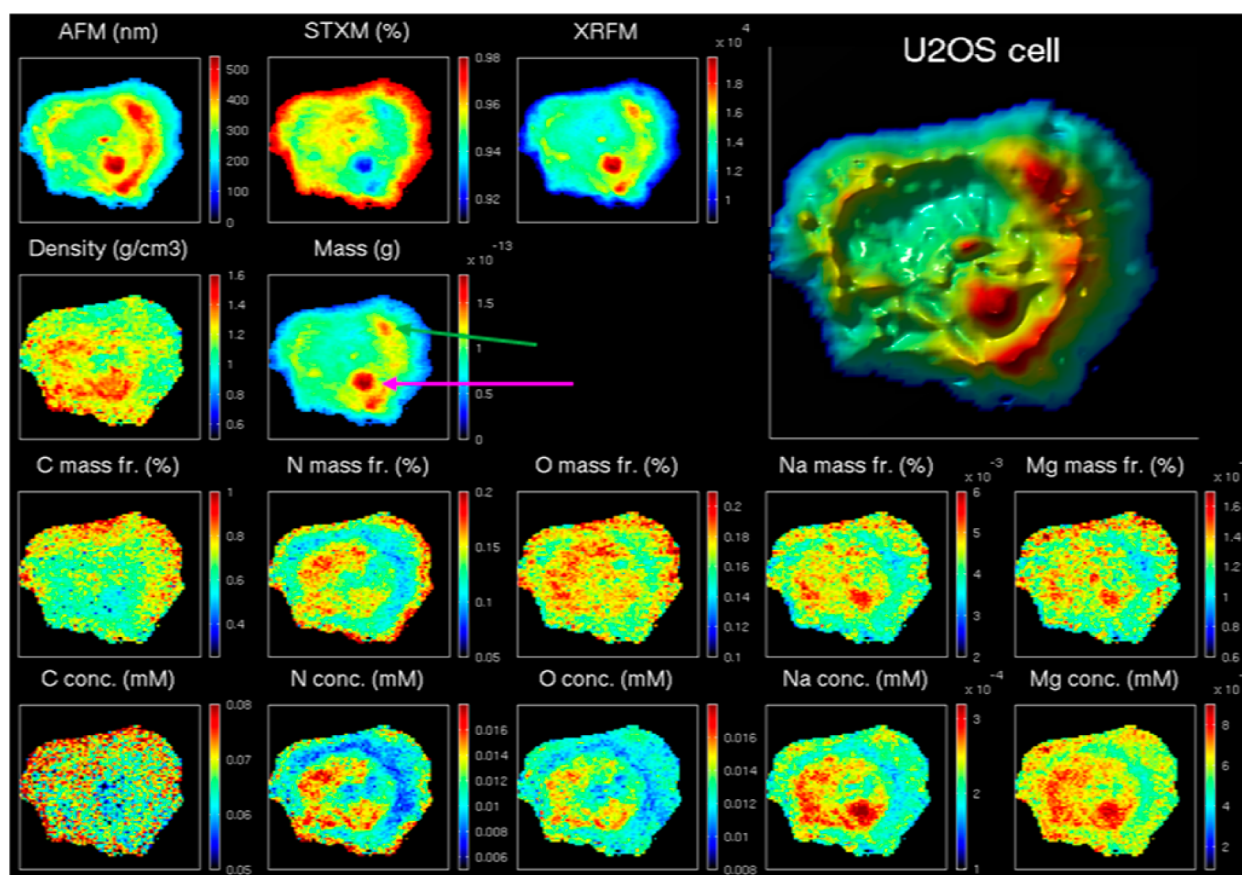
Figure 2. (Top row, from the left) morphology, X-ray transmission, and X-ray fluorescence images of a dehydrated human osteosarcoma cell U2OS, acquired by atomic force microscopy (AFM), scanning transmission X-ray microscopy (STXM), and X-ray fluorescence microscopy (XRFM), respectively. The XRFM image reports the sum of all the channels of the spectrum. In the top right panel a 3D rendering of AFM is shown. A map of the spatial distribution of the cell density and mass is then calculated from AFM and STXM (second row). Arrows indicate the areas where mass and density intracellular distributions markedly differ. The third and fourth rows show elemental maps of mass fraction and molar concentration of C, N, O, Na, and Mg.

The concentration maps of the various elements showed different patterns: those of sodium and magnesium were the most comparable to the density map, while the most dissimilar was that of carbon. Moreover, there were differences between mass fraction and concentration maps of all the elements, those of oxygen being the most divergent.

It must be noted that mass fraction is a dimensionless quantity expressed in percent with respect to total mass. In fact, in eq 5 the volumetric information contained in the density variable is simplified by multiplying by the volume of each pixel (term V_p in eq 5).

On the other hand, the concentration is an intensive property and the molar concentration map provides the actual intracellular volumetric distribution of the moles of each element. Molar concentration represents the appropriate information, since chemical reactions are expressed in terms of moles. This is the first study to achieve molar concentration maps of light elements and light metals in whole single cells.

Self-Absorption Correction. The fundamental parameter equations (eqs 3 and 5, Experimental Section) contain an expression for the self-absorption correction, which is an essential prerequisite to obtain the quantitative maps of light elements and hence one of the key steps of our analytical procedure. It is worth noting that eq 6 is a modified version of the fundamental parameter equation (eq 5) simplified for the density ρ. The use of eq 6 implies two major peculiarities: (i)

molar concentration can be calculated by bypassing the calculation of mass fraction and (ii) in the case of the concentration assessment of non-light elements, for which the term $I_0 \exp(-\chi\rho z)$ can be omitted as they do not require the self-absorption correction, the density calculation is not even required. However, the volumetric information coming from AFM is still necessary.

In Figure S2 of Supporting Information, we show the raw fluorescence maps. The different position of the eight detectors concentrically mounted at a 20° grazing angle to the specimen plane (Figure S1, Supporting Information) causes an asymmetric fluorescence pattern due to the different path that the emitted photons have to traverse through the cell. The asymmetry disappears in the corrected maps (Figure S2 of Supporting Information). The correction has been carried out with an "ad hoc" algorithm[15] (see Experimental Section) that exploits the information on morphology obtained by the AFM measurements.

Absolute Quantification and Error Analysis. We want to stress that, by merging XRFM, STXM, and AFM measurements, an absolute quantification of structural (density, mass, and volume) and compositional (mass fraction, concentration) properties is obtained. It is therefore of extreme importance to evaluate the uncertainty in quantification (see Supporting Information). In the Experimental Section we report a careful analysis of the uncertainty of all the relevant
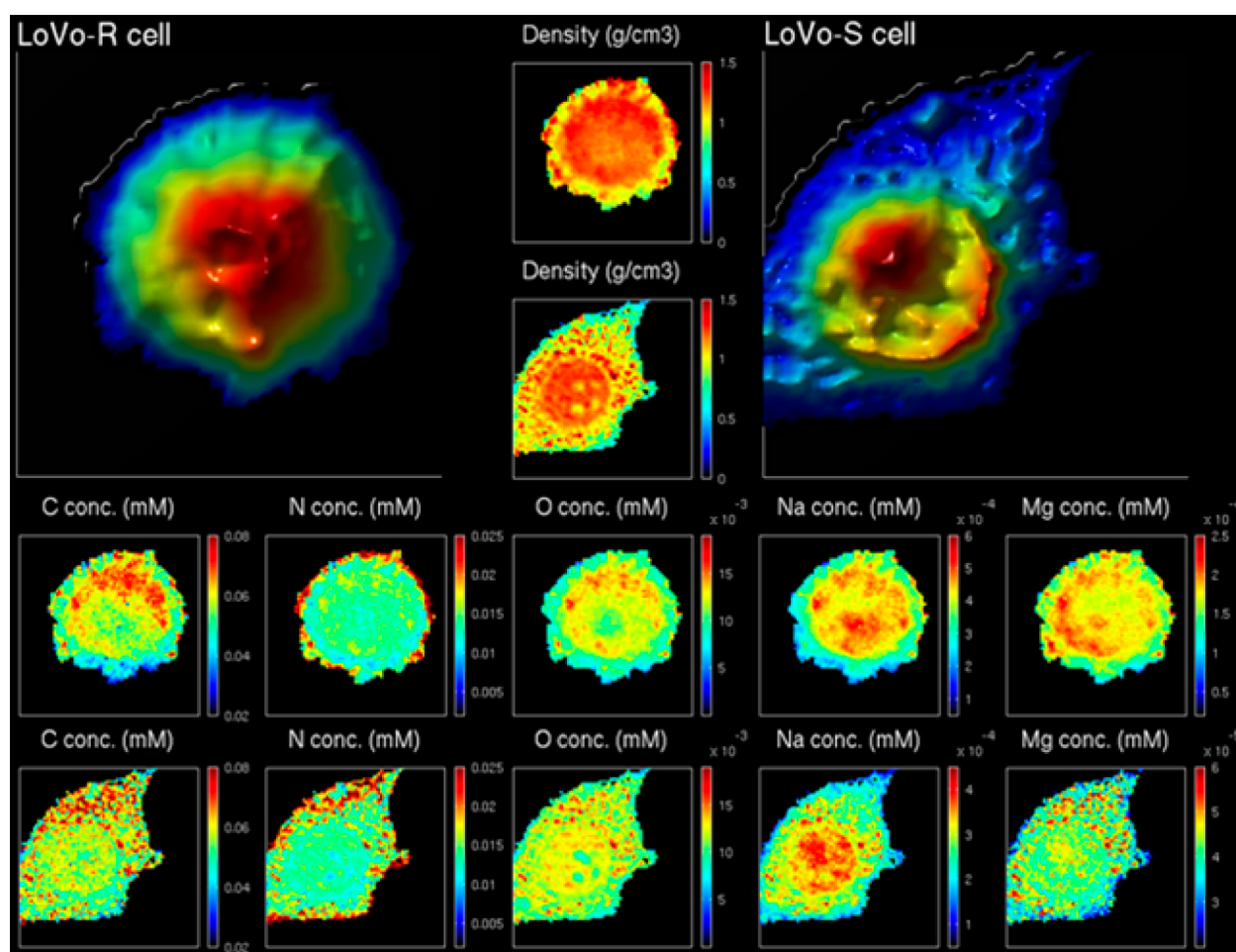
Figure 3. (Upper panel) AFM 3D renderings of a dehydrated human colon carcinoma LoVo-R cell (left) and a LoVo-S cell (right) (cells 4 and 1 reported in Table 1). The respective density maps are reported in between. The correspondence is evident by cell morphology. (Lower panel) Concentration maps of C, N, O, Na, and Mg for the LoVo-R cell (upper row) and for the LoVo-S cell (lower row).

quantities. As an example, Figure S3 in Supporting Information shows the relative uncertainty of density, oxygen mass fraction, and oxygen molar concentration of U2OS cell. Similar maps were drawn for all the elements and for all the cells. It can be noted that the relative uncertainty is always in the range 10–30%, except in the far periphery of the cell, where the relative uncertainty is higher due to the smaller thickness. This is not surprising, since the lower the thickness, the higher the uncertainty in fluorescence and AFM measurements. A threshold of 30% relative uncertainty in the single pixel for the maps of density, mass fraction, and molar concentration maps of C, N, O and Na was taken. Since Mg has a low intracellular concentration, the mass fraction and concentration maps of this element were generated with a relative uncertainty threshold of 50%.

Different Mg Intracellular Distribution in Drug-Sensitive and -Resistant Cancer Cells. To test the applicability of our analytical method on a challenging biological issue, we performed measurements on LoVo cells sensitive (LoVo-S) or resistant (LoVo-R) to doxorubicin. Doxorubicin is frequently employed as an anticancer drug, but resistance to doxorubicin often occurs and remains the main obstacle to the success of the therapy. Resistance is a multifactorial phenomenon involving several biochemical processes, which also implies intracellular ionic concentration changes. Three LoVo-S and two LoVo-R cells were dehydrated

by use of a cold mixture of methanol and acetone (chemically fixed), while two LoVo-S cells were freeze-dried by cryofixation (see Experimental Section for details of cell preparation).

The comparison between LoVo-S and LoVo-R cells revealed different patterns in the spatial distribution of molar Mg concentration (Figure 3). LoVo-R cells displayed the highest values of molar Mg concentration within the nucleus, while LoVo-S cells showed the highest values in the perinuclear region. This feature was not evident for the other elements, suggesting that Mg compartmentalization could be a significant trait of the drug-resistant cells.

How Different Dehydration Methods Affect Intracellular Morphology. Figure S4 in Supporting Information shows the comparison between chemically fixed and freeze-dried cells. Notable differences in the spatial distribution of all the elements are evident. All the freeze-dried cells showed a more heterogeneous elemental distribution mirroring the subcellular structures. In freeze-dried cells, a perinuclear ring was particularly evident that corresponded with the endoplasmic reticulum with low values of density and concentration for all the elements. This ring is not visible in the chemically fixed cells, suggesting a more invasive impact of this dehydration method in respect to cryofixation.[8]

Whole Cell Quantification. Once maps of density, mass, mass fraction, and molar concentration are calculated, the local information on spatial distribution has to be complemented by

Table 1. Whole Cell Parameters[a]

cell	density (g/cm^3)	volume (μm^3)	mass (pg)	C (mM)	N (mM)	O (mM)	Na (mM)	Mg (mM)	W_C (%)	W_N (%)	W_O (%)	W_{Na} (%)	W_{Mg} (%)	W_{tot} (%)
1, LoVo-S	1.11	171	190	56130	13264	12079	323	43	61	18	17	0.66	0.09	97
2, LoVo-S	1.25	203	254	64165	15105	12370	508	32	62	17	16	0.93	0.06	96
3, LoVo-S	1.10	114	125	64493	14404	12130	239	13	70	17	17	0.49	0.03	105
4, LoVo-R	1.17	434	508	57693	13875	11794	414	176	59	17	16	0.81	0.36	93
5, LoVo-R	1.12	175	195	58300	11563	10272	425	176	63	15	15	0.87	0.38	94
6, LoVo-S*	1.06	257	271	51047	11944	12142	147	77	59	17	18	0.32	0.18	95
7, LoVo-S*	1.14	344	392	48950	11188	11392	161	88	53	14	16	0.33	0.19	84
8, U2OS*	1.20	248	297	67554	11442	12887	229	63	68	14	17	0.44	0.13	99
mean	1.14	243	279	58542	12848	11883	306	84	62	16	17	0.61	0.18	95
SD	0.06	103	122	6580	1509	780	133	62	5	2	1	0.24	0.13	6
CV (%)	5	43	44	11	12	7	43	74	9	10	6	40	74	6

[a]For each cell, total volume calculated from AFM and total mass and mean density calculated from the respective mass and density maps are reported. The calculated mass fraction (W) and concentration of each element are also reported for each cell. The sum of mass fractions of all the elements (total mass fraction W_{tot}) was also calculated. Asterisks denotes cryofixed cells. SD, standard deviation; CV, coefficient of variation.

quantitative global information on the whole cell. The combination of local and global information allows a sort of fingerprint identification of the single-cell features. Therefore, we calculated the whole cell volume, mass, density, and elemental mass fraction and molar concentration (Table 1). We also calculated the sum of the mass fractions of all the elements (total mass fraction W_{tot}). All the values reported in Table 1 were taken by superimposing thresholds as reported above in the previous section. Mean values, standard deviation, and coefficient of variation calculated for the ensemble of all the cells are also reported in Table 1. We show the results for cells mentioned in previous sections and in particular (i) human osteosarcoma U2OS freeze-dried by cryofixation, (ii) human colon cancer cells LoVo-S and LoVo-R, either chemically fixed or freeze-dried. The freeze-dried samples are marked with asterisks in Table 1).

All the cells showed similar mean density values despite the method of fixation and the different total volume and mass. Note the very low standard deviation and coefficient of variation in density, compared to the corresponding values in mass and volume (Table 1). The values of W_{tot} were all but one close to 90% and below 100% as we did not measure the amount of hydrogen and phosphorus, which, according to literature,[13] account for about 7−10%. The concentration and the mass fraction of C, N, and O did not present significant variations in the eight cells measured, while the light metals Na and particularly Mg displayed much greater variations. In particular, LoVo-R cells showed a relevant increase of Mg molar concentration and mass fraction compared to LoVo-S. This, together with the different compartmentalization of Mg (see previous section on Mg intracellular distribution), represents a very intriguing result as there is experimental evidence suggesting that Mg is involved in the mechanism of drug resistance[17,18] and a higher Mg concentration has been found in cisplatin drug-resistant human ovarian cancer cells.[9] Regarding the different preparation procedures, it can be noted that there are no significant differences in the mean values of total element mass fraction and concentration between chemically fixed and freeze-dried cells, despite the notable differences in their element concentration maps (Figure S4 in Supporting Information).

■ CONCLUSION

The study was performed on dried cells. Indeed, this represents the only practicable choice since the use of frozen hydrated cells could have precluded the possibility to quantify and map the FLE because the oxygen signal coming from water would have eclipsed the oxygen signal pertaining to organic molecules. In working with dried cells, an important issue to consider is the damage by radiation, as the dose the cells are subjected to is quite relevant (about 2.5×10^8 Gy) and dried cells are more radiation-sensitive than frozen hydrated cells. However, by repeating the fluorescence measurements on the same cell, we had clear indications that neither cell density nor concentration of elements showed a detectable change, with the sole exception of oxygen, whose concentration decreased by only a few percent after the second exposure. Also, AFM measurements taken after the X-ray measurements did not show detectable volume differences when compared to those taken before and after. Therefore, if no volume and density changes were revealed, it can be concluded that no mass loss during the XRFM experiments occurred.

In conclusion, we have reported a novel method that allows for the first time a quantitative mapping at the submicrometer level of fundamental life elements C, N, and O and light metals Na and Mg in whole cells. This result was obtained by applying a multimodal fusion approach that combines synchrotron radiation microscopy techniques with off-line AFM. Precise knowledge of the cell morphology allows us to carry out correction for self-absorption, which is absolutely necessary to obtain quantitative compositional information on FLE and light metals. It is worth noting that the method proposed in this study permits us to map the element molar concentration in addition to mass fraction, because it provides volumetric information with AFM. Quantitative mapping of density is obtained by use of STXM at 1475 eV, which provides a detailed X-ray transmission map with good contrast for cell structure. At this energy it is therefore not necessary to use phase contrast imaging, different from measurements at higher energy.[19] The present work is focused on light elements but can be obviously extended to heavier elements, like Fe, Zn, Cu, etc.

In this study spatial resolution is limited to about 500 nm. Better spatial resolution can be achieved in most of the beamlines dedicated to XRFM, including the one used in this work. A tradeoff between spatial resolution, measurement time,

and radiation damage must be found, however. To this purpose we would stress the need for an efficient X-ray fluorescence detector.

Cellular processes are driven by concentration gradients, and a map of the elemental intracellular concentration represents new information obtainable only by this analytical approach. Indeed, the different intracellular Mg content and spatial distribution found in drug-resistant cells with respect to their drug-sensitive counterpart provides preliminary information useful in the investigation of ion involvement in the multidrug resistance phenomenon.

We stress the importance of quantitative mapping of FLE and light metals in cells at high spatial resolution, a result never achieved before. This possibility allows a more in-depth study of the relationship between structure and function at the subcellular level and opens new perspectives in different fields of research. For example, several recent studies are related to analysis of oxygen consumption and distribution.[20−22] The opportunity to quantify total oxygen and its distribution, not only in cultured cells but also in primary ones, is certainly a fascinating option with unforeseen consequences. A further relevant application offered by this approach is the quantitative mapping of any type of nanocomposites in biological systems since XRFM is currently employed in nanoparticle mapping and speciation.[16,23] Furthermore, the possibility of quantifying light elements opens the interesting perspective to extend the application to intracellular mapping of carbon-based nanoparticles (for example, carbon nanotubes), which represent the new frontier in the development of advanced drug delivery systems.[24]

■ ASSOCIATED CONTENT

Ⓢ Supporting Information

Additional text discussing error analysis and four figures showing experimental set-up at Twinmic beam line at Elettra; raw and corrected X-ray fluorescence maps; maps of relative uncertainties for density, oxygen mass fraction, and oxygen molar concentration; and AFM 3D rendering and concentration maps of C, N, O, Na, and Mg. This material is available free of charge via the Internet at http://pubs.acs.org.

■ AUTHOR INFORMATION

Corresponding Author

*E-mail stefano.iotti@unibo.it; fax +39 051 2091234.

Notes

The authors declare no competing financial interest.

■ ACKNOWLEDGMENTS

■ REFERENCES

(1) Ortega, R.; Devès, G.; Carmona, A. *J. R. Soc., Interface* **2009**, *6*, S649−S658.

(2) Moore, K. L.; Lombi, E.; Zhao, F.; Grovenor, C. R. M. *Anal. Bioanal. Chem.* **2012**, *402*, 3263−3273.

(3) De Jonge, M. D.; Holzner, C.; Baines, S. B.; Twining, B. S.; Ignatyev, K.; Diaz, J.; Howard, D. L.; Legnini, D.; Miceli, A.; McNulty, I.; Jacobsen, C. J.; Vogt, S. *Proc. Natl. Acad. Sci. U.S.A.* **2010**, *107*, 15696−15680.

(4) Corezzi, S.; Urbanelli, L.; Cloetens, P.; Emiliani, C.; Helfen, L.; Bohic, S.; Elisei, F.; Fioretto, D. *Anal. Biochem.* **2009**, *388*, 33−39.

(5) Lagomarsino, S.; Iotti, S.; Farruggia, G.; Cedola, A.; Trapani, V.; Fratini, M.; Bukreeva, I.; Notargiacomo, A.; Mastrototaro, L.; Marraccini, C.; Sorrentino, A.; McNulty, I.; Vogt, S.; Legnini, D.; Kim, S.; Gianoncelli, A.; Maier, J.; Wolf, F. I. *Spectrochim. Acta, Part B* **2011**, *66*, 834−840.

(6) Farruggia, G.; Iotti, S; Prodi, L; Zaccheroni, N.; Montalti, M.; Savage, P. B.; Andreani, G.; Trapani, V.; Wolf, F. I. *J. Fluoresc.* **2009**, *19*, 11−19.

(7) Janssens, K. H. A.; Adams, F. C. V.; Rindby, A. *Microscopic X-ray Fluorescence Analysis*; John Wiley & Sons Ltd: New York, 2000; pp 171−190.

(8) Carmona, A.; Devès, G.; Ortega, R. *Anal. Bioanal. Chem.* **2008**, *390*, 1585−1594.

(9) Marverti, G.; Ligabue, A.; Montanari, M.; Guerrieri, D.; Cusumano, M.; Di Pietro, M. L.; Troiano, L.; Di Vono, E.; Iotti, S.; Farruggia, G.; Wolf, F. I.; Monti, M. G.; Frassineti, C. *Invest. New Drugs* **2011**, *29*, 73−86.

(10) Kaulich, B.; Bacescu, D.; Susini, J.; David, C.; Di Fabrizio, E.; Morrison, G. R.; Charalambous, P.; Thieme, J.; Wilhein, T.; Kovac, J.; Cocco, D.; Salome, M.; Dhez, O.; Weitkamp, T; Cabrini, S.; Cojoc, D.; Gianoncelli, A.; Vogt, U; Podnar, M.; Zangrando, M.; Zacchigna, M.; Kiskinova1, M. *IPAP Conf. Ser.* **2006**, *7*, 22−25.

(11) Gianoncelli, A.; Kaulich, B.; Alberti, R.; Klatka, T.; Longoni, A.; De Marco, A.; Marcello, A.; Kiskinova, M. *Nucl. Instrum. Methods A* **2009**, *608*, 195−198.

(12) Gianoncelli, A.; Morrison, G. R.; Kaulich, B.; Bacescu, D.; Kovac, J. *Appl. Phys. Lett.* **2006**, *89*, No. 251117.

(13) Von Stockar, U.; Liu, J. *Biochim. Biophys. Acta* **1999**, *1412*, 191−211.

(14) Solé, V. A.; Papillon, E.; Cotte, M.; Walter, P. H.; Susini, J. *Spectrochim. Acta, Part B* **2007**, *62*, 63−68.

(15) Malucelli, E.; Iotti, I.; Fratini, M.; Marraccini, C.; Notargiacomo, A.; Gianoncelli, A.; Bukreeva, I.; Cedola, A.; Maier, J.; Farruggia, G.; Cappadone, C.; Merolle, L.; Wolf, F.; Trapani, V.; Lagomarsino, S. *J. Phys. Conf. Ser.* **2013**, *463*, No. 012022.

(16) Hernandez-Viezcas, J. A.; Castillo-Michel, H.; Andrews, J. C.; Cotte, M.; Rico, C.; Peralta-Videa, J. R.; Ge, Y.; Priester, J. H.; Holden, P. A.; Gardea-Torresdey, J. L. *ACS Nano* **2013**, *7*, 1415−1423.

(17) Chen, Y.; Wei, X.; Yan, P.; Han, Y.; Sun, S.; Wu, K.; Fan, D. *Cancer Biol. Ther.* **2009**, *8*, 607−614.

(18) Wolf, F. I; Trapani, V. *Cancer Biol. Ther.* **2009**, *8*, 615−617.

(19) Kosior, E.; Sylvain, B.; Suhonen, H.; Ortega, R.; Devès, G.; Carmona, A.; Marchi, F.; Guillet, J. F.; Cloetens, P. *J. Struct. Biol.* **2012**, *177*, 239−247.

(20) Wang, X.; Gorris, H. H.; Stolwijk, J. A.; Meier, R. J.; Groegel, D. B. M.; Wegenera, J.; Wolfbeis, O. S. *Chem. Sci.* **2011**, *2*, 901−906.

(21) Molter, T.; McQuaide, S. C.; Holl, M. R.; Meldrum, D. R.; Dragavon, J. M.; Anderson, J. B.; Young, A. C.; Burgess, L. W.; Lidstrom, M. E. *IEEE Trans. Autom. Sci. Eng.* **2008**, *5*, 32−42.

(22) O'Riordan, T. C.; Zhdanov, A. V.; Ponomarev, G. V.; Papkovsky, D. B. *Anal. Chem.* **2007**, *79*, 9414−9419.

(23) Fahmi, C. J. *Curr. Opin. Chem. Biol.* **2007**, *11*, 121−127.

(24) Bhirde, A. A.; Patel, V.; Gavard, J.; Zhang, G.; Sousa, A. A.; Masedunskas, A.; Leapman, R. D.; Weigert, R.; Gutkind, J. S.; Rusling, J. F. *ACS Nano* **2009**, *3*, 307−316.